energies

MDPI

Article

Robust Eddy Viscosity Turbulence Modeling with Elliptic Relaxation and Compound Wall Treatment

Mirza Popovac

AIT-Austrian Institute of Technology, Electric Vehicle Technologies, Center for Low-Emission Transport, Giefinggasse 2, 1210 Vienna, Austria; mirza.popovac@ait.ac.at

Abstract: This paper presents a holistic Reynolds-averaged Navier–Stokes (RANS) turbulence modeling framework for the computational fluid dynamics (CFD) simulations of complex wall-bounded turbulent flows. Based on the elliptic relaxation idea, the deployed eddy viscosity turbulence model reconstructs the near-wall stress anisotropy and nonviscous effects. The appropriate selection of the turbulent quantities that are being solved for, together with the zero value wall boundary condition for the related turbulent quantities, renders the model less sensitive to the near-wall grid nonuniformities and resolution. The unified near-wall velocity profile, obtained based on the boundary layer theory, is used to devise the compound near-wall treatment that ensures the robustness of the numerical simulation. The proposed turbulence modeling framework is implemented into the general-purpose open-source CFD code and validated against the generic test cases with satisfactory agreement.

Keywords: computational fluid dynamics (CFD); Reynolds-averaged Navier–Stokes (RANS) turbulence modeling; wall functions

Citation: Popovac, M. Robust Eddy Viscosity Turbulence Modeling with Elliptic Relaxation and Compound Wall Treatment. *Energies* **2023**, *16*, 3685. https://doi.org/10.3390/en16093685

Academic Editor: F. Xavier Trias

Received: 27 February 2023
Revised: 20 April 2023
Accepted: 22 April 2023
Published: 25 April 2023

1. Introduction

The accuracy of computational fluid dynamics (CFD) simulations applied to the turbulent wall-bounded flows is determined by the correct physical description of wall-related fluid flow effects. Furthermore, in this case, the boundary layer needs to be sufficiently resolved, since most of the flow variation takes place in a thin region in the immediate vicinity of the solid boundary. In this regard, there are highly accurate yet computationally very demanding and time-consuming modeling approaches, such as large-eddy simulation (LES), which are based on resolving the energy-containing eddies and modeling only the interaction between the smallest flow scales [1]. Here, different rationales can be used for subgrid-scale modeling, such as the viscosity type of Smagorinsky [2], the dynamic Smagorinsky [3] or the structure function [4]. In an attempt to reduce the computation cost, more recent trends in wall-bounded flows turbulence modeling range from hybrid approaches (which blend the eddy-resolving and eddy interaction modeling procedures [5]) to emerging machine learning approaches (where deep neural networks are used to train the replacing elements of the fluid flow interaction at scales that are affected by the loss of resolution [6]).

This paper is restricted to the conventional Reynolds-averaged Navier–Stokes (RANS) approach which, due to its moderate mesh requirements, results in much lower computation time and resources demand. In this statistical approach, the turbulent interaction is modeled across the entire range of flow scales. Looking at the standard $k-\varepsilon$ model [7], which is widely used in the engineering practice, the turbulent motion is characterized through the turbulent kinetic energy k and its dissipation rate ε. The deficiency of this model is its isotropic nature, which is inappropriate for capturing wall effects. Moreover, it is not designed to resolve the near-wall region; instead, the wall functions are used for bridging the flow region in the wall vicinity. Early attempts to correct this shortcoming were based on empirical near-wall damping functions [8]. To obviate the need for damping

functions, Durbin [9] introduced (in addition to k and ε) the wall-normal Reynolds stress component $\overline{v^2}$ as the turbulent velocity scale, which is sensitized to inviscid wall-blocking effects through the elliptic relaxation function f. Although the original $\overline{v^2} - f$ model significantly improved the CFD predictions of wall-bounded flows, its applicability in complex engineering problems was hampered by the stiff boundary conditions and thus related near-wall behavior and mesh sensitivity.

After Durbin's elliptic relaxation near-wall model was presented, a number of modifications were proposed in the literature aiming to improve the model's numerical performance. Lien et al. [10] reformulated the definition of the elliptic relaxation function in order to obtain the zero value boundary condition, and even though the resulting formulation is not identical to the original one, this certainly improves the computation stability of the model. Durbin [11] put under scrutiny the turbulent time and length scale, deriving constraints in order to assure their appropriate behavior under different flow conditions. Davidson et al. [12] proposed the turbulent velocity scale to be controlled by the equilibrium value; however, in addition to rather rude implementation, this attempt does not provide entirely correct behavior.

In order to overcome the weakness of the $\overline{v^2} - f$ model, Popovac and Hanjalic derived the $\zeta - f$ modification of Durbin's eddy viscosity model [13], in which the transport equation for the velocity scale ratio $\zeta = \overline{v^2}/k$ is solved instead of the equation for $\overline{v^2}$. With this change, the power of a variable's variation near the wall is reduced, which has a positive impact on the sensitivity of the model. Furthermore, the application of an advanced quasi-linear pressure–strain model in the equation for the elliptic relaxation function was introduced, resulting in better numerical stability when solving the transport equation for the new velocity scale ratio (as compared with its parent transport equation). In conclusion, in order to derive a modeling approach suitable for complex engineering computations, the authors discussed the unified near-wall treatment with a pragmatic implementation of the wall boundary conditions [14].

With the aim to provide a high accuracy of numerical simulations for complex engineering flow problems at reasonably low computational cost, this paper presents a holistic near-wall turbulence modeling approach with the advantages of the numerically stable simulation of complex near-wall turbulent flow physics, as well as robust performance regarding the mesh requirements for the wall boundary and initial flow conditions. As a gap-filling novelty, this modeling framework includes a physically sound near-wall treatment, which ensures adequate closure irrespective of the near-wall mesh quality and resolution. Following this introductory overview, the subsequent sections introduce the formulation of the proposed turbulence modeling framework. Section 2 gives the fluid flow governing equations and the basic concept of turbulence modeling, with more details of the developed wall-bounded flow turbulence model provided in Section 2.1 and the near-wall treatment in Section 2.2. The presented approach was implemented into an open-source CFD solver, and its performance tested on generic flow cases which feature relevant near-wall flow effects. In Section 3, a comparison between the obtained results and the reference measurements or numerical data for the plane shear flow (Section 3.1), the two-dimensional separating flow (Section 3.2), and the axisymmetric impinging jet (Section 3.3) is given. The paper closes with the discussion and conclusions in Section 4.

2. Governing Equations

The isothermal incompressible turbulent flow of Newtonian fluid is governed by the Navier–Stokes equations, describing the conservation of mass and momentum. By decomposing the instantaneous turbulent flow quantities into the mean and fluctuating part ($\tilde{\phi} = \Phi + \phi$) and subsequently applying the Reynolds averaging procedure ($\overline{\tilde{\phi}} = \overline{\Phi + \phi}$),

the system of equations that yields the mean flow velocity vector U_i and the pressure P is obtained [15]:

$$\begin{aligned} \frac{\partial U_i}{\partial x_i} &= 0 \\ \frac{\partial U_i}{\partial t} + U_j \frac{\partial U_i}{\partial x_j} &= -\frac{1}{\rho}\frac{\partial P}{\partial x_i} + \nu \frac{\partial^2 U_i}{\partial x_j \partial x_j} - \frac{\partial \overline{u_i u_j}}{\partial x_j} \end{aligned} \tag{1}$$

where ρ is the fluid density, ν is the kinematic fluid viscosity, and $\overline{u_i u_j}$ is the *Reynolds* or *turbulent stress* tensor (Einstein notation applies for indices i and j).

Arising from the Reynolds averaging of the convective term in the momentum equation, the second moment tensor $\overline{u_i u_j}$ represents the effects of turbulent motion on the mean flow. Namely, due to nonlinear interaction between the velocity components in the Navier–Stokes equations (Equation (1)), in addition to the first moment (mean), the Reynolds-averaged equations also include the second moment (covariance). This leads to the closure problem for the Reynolds-averaged equations: the Reynolds stress needs to be expressed through the mean flow variables and related turbulent quantities that characterize the flow. The linear model for Reynolds stress tensor, using the Boussinesq assumption [16], reads:

$$-\overline{u_i u_j} = 2\nu_t S_{ij} - \frac{2}{3} k \delta_{ij} \tag{2}$$

where the average kinetic energy of the velocity fluctuations $k = \frac{1}{2}\overline{u_i u_i}$ contributes to the isotropic part of the tensor (δ_{ij} is the Kronecker delta), and the deviatoric part of the tensor is proportional to the mean rate-of-strain tensor $S_{ij} = \frac{1}{2}\left(\frac{\partial U_i}{\partial x_j} + \frac{\partial U_j}{\partial x_i}\right)$, with the coefficient of proportionality ν_t being the kinematic *eddy* or *turbulent viscosity*. Using Equation (2), the final form of the momentum equation reads:

$$\frac{\partial U_i}{\partial t} + U_j \frac{\partial U_i}{\partial x_j} = -\frac{1}{\rho}\frac{\partial P}{\partial x_i} + \frac{\partial}{\partial x_j}\left[\underbrace{(\nu + \nu_t)}_{\nu_{eff}}\left(\frac{\partial U_i}{\partial x_j} + \frac{\partial U_j}{\partial x_i}\right)\right] \tag{3}$$

with the effective momentum diffusivity $\nu_{eff} = \nu + \nu_t$ comprising the kinematic and turbulent viscosity.

2.1. Turbulence Model

The eddy viscosity idea for the Reynolds stress modeling is introduced in analogy to the viscous stress: just like the fluid viscosity is proportional to the mean free path and mean speed of molecules, the turbulent viscosity is a function of the characteristic turbulent velocity and length scale. The analogy ends with the dimensional consistency, however, because ν is the property of the fluid, while ν_t is the property of the flow. In the two-equation eddy viscosity modeling approach, the turbulent contribution to the effective momentum diffusivity is obtained from the transport equations for two turbulent quantities: one for calculating the velocity scale $\mathcal{V}$ and the other for defining the time scale of turbulent motion $\mathcal{T}$ (yielding thus the length scale $\ell = \mathcal{V}\mathcal{T}$). In the present work, the turbulent quantities required for the definition of the turbulent viscosity ν_t are devised within the $k - \varepsilon$ turbulence model family:

$$\nu_t = c_\mu k \mathcal{T} \frac{\zeta}{\zeta_{eq}} \tag{4}$$

where the turbulent kinetic energy k is used for defining the characteristic time scale ($\mathcal{T} \sim \frac{k}{\varepsilon}$) and velocity scale ($\mathcal{V}^2 \sim k$):

$$\frac{\partial k}{\partial t} + U_j \frac{\partial k}{\partial x_j} = \mathcal{P} - \varepsilon + \frac{\partial}{\partial x_j}\left[\left(\nu + \frac{\nu_t}{\sigma_k}\right)\frac{\partial k}{\partial x_j}\right] \tag{5}$$

together with the turbulent kinetic energy dissipation rate ε:

$$\frac{\partial \varepsilon}{\partial t} + U_j \frac{\partial \varepsilon}{\partial x_j} = \frac{C_{\varepsilon 1}\mathcal{P} - C_{\varepsilon 2}\varepsilon}{\mathcal{T}} + \frac{\partial}{\partial x_j}\left[\left(\nu + \frac{\nu_t}{\sigma_\varepsilon}\right)\frac{\partial \varepsilon}{\partial x_j}\right] \tag{6}$$

whereby $\mathcal{P} = -\overline{u_i u_j}\frac{\partial U_i}{\partial x_j}$ is the production of the turbulent kinetic energy, and the normalized fluctuating velocity ζ provides the correct near-wall behavior of ν_t, while c_μ, σ_ε, σ_k, $C_{\varepsilon 1}$, $C_{\varepsilon 2}$, and ζ_{eq} are the model coefficients.

The production of the turbulent kinetic energy, typically calculated as $\mathcal{P} = \nu_t S^2$, using the modulus of the mean rate-of-strain tensor $S = \sqrt{2S_{ij}S_{ij}}$, quantifies the kinetic energy of the mean flow transferred to the turbulent stresses. While the transport equation for k (Equation (5)) can be derived exactly from the Reynolds stress equations, the ε transport equation (Equation (6)) is constructed to have the same form as for k (only scaled with appropriate time scale, following the definition of ε). As for the model coefficients, $C_{\varepsilon 1} = C'_{\varepsilon 1}(1 + C''_{\varepsilon 1}/\sqrt{\zeta})$ accounts for a sharp variation of the dissipation rate in the near-wall vicinity, and all other model coefficients are summarized in Table 1.

Table 1. The $\zeta - f_0$ model coefficients.

c_μ	σ_k	σ_ε	σ_ζ	$C'_{\varepsilon 1}$	$C''_{\varepsilon 1}$	$C_{\varepsilon 2}$	C_{f1}	C_{f2}	C_T	C_τ	C_L	C_η	ζ_{eq}	N_ζ	n_b
0.09	1.0	1.3	1.2	1.4	0.012	1.9	0.4	0.65	0.6	6.0	0.36	85	0.41	2	10/3

Durbin [9] noted that using the wall-normal fluctuating velocity component $\overline{u_2 u_2} = \overline{v^2}$ as the velocity scale, the correct near-wall behavior of turbulent viscosity for wall-bounded flows is recovered (here, the indices convention for u_i and x_i is used: $u_1 = u$, $x_1 = x$, streamwise direction; $u_2 = v$, $x_2 = y$, wall-normal direction; and $u_3 = w$, $x_3 = z$, spanwise direction). For this purpose, he derived the transport equation for $\overline{v^2}$ and introduced the elliptic relaxation function f for pressure–strain modeling as an essential element for describing the nonviscous near-wall effects. Although the $\overline{v^2} - f$ model brought significant improvements in the prediction accuracy, since it resembles the Reynolds stress approach in the direction normal to the streamlines, its near-wall mesh quality requirements remained excessively high, and the overall model performance is sensitive to the near-wall grid clustering. Aiming at easing the mesh requirements of the original Durbin model, Hanjalic and Popovac derived the $\zeta - f$ modification [13] by introducing the normalized fluctuating velocity in the direction normal to the streamlines $\zeta = \overline{v^2}/k$. In the transport equation transformation from $\overline{v^2}$ to ζ, the cross-diffusion term is omitted, and its effect (restricted only to the flow region very close to the wall) is compensated through the coefficient fine-tuning. Furthermore, following the SSG formulation of Speziale et al. [17], the quasi-linear pressure–strain model is applied in the elliptic relaxation function, as it better captures the stress anisotropy in wall boundary layers (as compared with the linear formulation based on the isotropization-of-production assumption).

In the present work, the $\zeta - f$ model is further reformulated in order to arrive at the zero value wall boundary condition for the relaxation function. To mark the difference, this reformulation is referred to as the $\zeta - f_0$ model. The adopted idea is outlined by Lien et al. [10], by which the fluctuating velocity transport equation is constructed with the contribution from the pressure fluctuation taken with the modifying model coefficient N_ζ:

$$\mathcal{L}^2 \nabla^2 f_0 - f_0 = \frac{\left(C_{f1} + C_{f2}\frac{\mathcal{P}}{\varepsilon}\right)\left(\zeta - \frac{2}{3}\right) + (N_\zeta - 1)\zeta}{\mathcal{T}} \tag{7}$$

$$\frac{\partial \zeta}{\partial t} + U_j \frac{\partial \zeta}{\partial x_j} = f_0 - \frac{\zeta\left[\frac{\mathcal{P}}{\varepsilon} + (N_\zeta - 1)\right]}{\mathcal{T}} + \frac{\partial}{\partial x_j}\left[\left(\nu + \frac{\nu_t}{\sigma_\zeta}\right)\frac{\partial \zeta}{\partial x_j}\right] \tag{8}$$

while the characteristic turbulent time and length scales, $\mathcal{T}$ and $\mathcal{L}$, respectively, are limited with the Kolmogorov values as the lower bounds and the realizability constraints as the upper bounds [15]:

$$\mathcal{T} = max\left[min\left(\frac{k}{\varepsilon}, \frac{C_T}{\sqrt{6}c_\mu|S|\zeta}\right), C_\tau\left(\frac{\nu}{\varepsilon}\right)^{1/2}\right] \tag{9}$$

$$\mathcal{L} = C_L\, max\left[min\left(\frac{k^{3/2}}{\varepsilon}, \frac{k^{1/2}}{\sqrt{6}c_\mu|S|\zeta}\right), C_\eta\left(\frac{\nu^3}{\varepsilon}\right)^{1/4}\right] \tag{10}$$

Looking at the $\zeta - f_0$ model set of coefficients (Table 1), note that Durbin introduced the turbulent viscosity coefficient $C_\mu = 0.22$, which is different from the standard $k - \varepsilon$ value $c_\mu = 0.09$ (also used here for the $\zeta - f_0$ model). C_μ differs from c_μ by the constant $\zeta_{eq} = 0.41$, which is the equilibrium value of ζ identified as the plateau in its wall-normal profile. In other words, the near-wall correction of the standard $k - \varepsilon$ turbulent viscosity is introduced through the ζ scaled to unity (Equation (4)). For completeness, from SSG comes an additional term in Equation (7), however, its coefficient being $C_{f3} = 0.008$, which is two orders of magnitude smaller than the other coefficients in the f_0 equation, it is safe to neglect it. Putting $N_\zeta = 1$ in the $\zeta - f_0$ formulation, the model reverts to its initial $\zeta - f$ form, whereby the case with zero value wall boundary condition is not identical to the nonzero value one (due to the elliptic nature of the relaxation function), but this alteration has a very limited effect on general mesh types (for which it is intended to be used).

2.2. Compound Wall Treatment

To complete the set of the $\zeta - f_0$ model equations (Equations (5)–(8)), the appropriate boundary conditions have to be provided. In the case of the *integration to the wall* (ItW) of the transport equations on a fine mesh, the exact boundary conditions are imposed on the solid boundary surface, while the mesh resolution applied near the wall recovers the sharp gradients of flow quantities occurring there. For insufficient near-wall mesh resolution, on the other hand, one has to assume certain fluid flow behaviors in the near-wall region, and from there derive the *wall functions* (WF) which will reconstruct the desired wall boundary condition on the coarse mesh [18]. Depending on the characteristics of the analyzed flow and geometry, it is probable that for a complex wall-bounded flow, the applied numerical mesh will involve both ItW and WF in different flow sections. This is where the *compound wall treatment* (CWT) comes into play to provide a continuous and accurate distribution of the flow quantities throughout the near-wall region, as is needed for the appropriate specification of the boundary conditions irrespective of the local mesh resolution [14].

For the approximation of the near-wall flow conditions, the fully developed 2D equilibrium turbulent boundary layer can be taken [19]. From the available experimental and numerical data, one can identify different flow regions with distinct velocity profiles: the inner sublayer, where the viscous forces dominate; the outer layer, where the inertial forces are dominant; and in between the buffer region, where both forces are equally significant. For the inner and outer flow regions (green dotted and dash-dotted lines, respectively, in Figure 1a), the normalized velocity profiles are given as:

$$U^+ = \frac{U}{u_\tau} = \begin{cases} U^+_{vis} = y^+ & \textit{viscous sublayer} \\ U^+_{log} = \frac{1}{\kappa} ln(Ey^+) & \textit{logarithmic layer} \end{cases} \tag{11}$$

where the friction velocity u_τ is the representative velocity scale for the wall shear stress, the Von Karman constant $\kappa = 0.41$ reflects the increment of the effective near-wall momentum diffusivity, $E = 8.9$ is the logarithmic constant related to the thickness of the viscous

sublayer, and y^+ is the normalized distance of the cell center to the solid boundary y_c, expressed in terms of the dimensionless wall units:

$$y^+ = \frac{y_c u_\tau}{\nu} \tag{12}$$

Following the differences between the inner sublayer (viscous dominated, extending up to approximately $y^+ < 5$) and outer logarithmic layer (inertia dominated, observed for approximately $y^+ > 30$), the friction velocity is defined as:

$$u_\tau = \begin{cases} u_\tau^{vis} = \sqrt{\frac{|\tau_w|}{\rho}} = \sqrt{\nu \frac{U_c}{y_c}} & \textit{viscous sublayer} \\ u_\tau^{log} = \sqrt{|\overline{uv}|} = c_\mu^{1/4} k_c^{1/2} & \textit{logarithmic layer} \end{cases} \tag{13}$$

either directly from the wall shear stress τ_w if the wall-adjacent cell center c lays within the viscous sublayer (resulting from the correct reconstruction of the velocity gradient, as the prerequisite for the correct τ_w), or indirectly through the Reynolds shear stress $\overline{uv}$ in case the near-wall cell is in the logarithmic layer (making use of the assumption that the wall shear stress τ_w is balanced with the turbulent shear stress $\overline{uv}$ in that region).

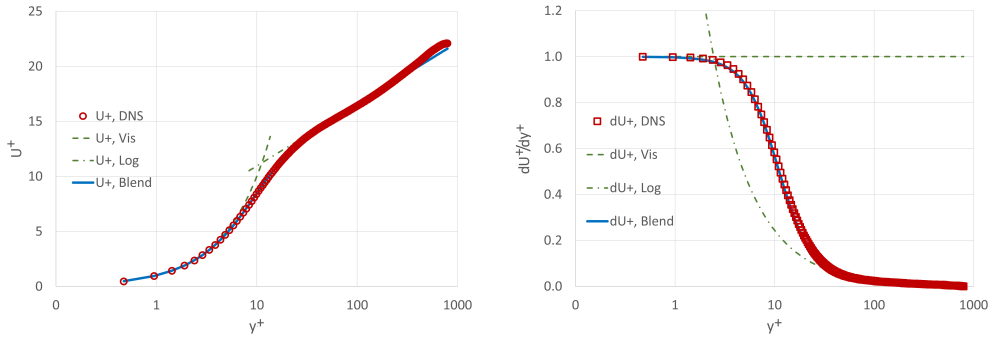

(**a**) (**b**)

Figure 1. Boundary layer flow distribution along dimensionless wall-normal distance y^+: (**a**) normalized velocity U^+ (U+) and (**b**) normalized velocity gradient dU^+/dy^+ (dU+).

The boundary layer velocity profile (Equation (11)) can be derived analytically in its generalized form by introducing in the momentum equation (Equation (3)) the boundary layer assumptions: the nonhomogeneity of the wall-tangent velocity component U is in the wall-normal direction y, the nonequilibrium effects are linearized (time variation, convection, and pressure gradient are known from the previous time step and constant throughout the near-wall cell), up to the viscous sublayer thickness y_v the effective momentum diffusivity reduces to the kinematic viscosity $\nu_{eff} = \nu$, while further into the boundary layer it linearly increases with the wall distance $\nu_{eff} = \kappa u_\tau y$. Thus, integrating Equation (3), after some mathematical manipulation (continuity and smoothness requirement for the integration constants), yields the wall shear stress when $y_c > y_v$ (coarse mesh):

$$\tau_w = \rho \frac{U_c - \frac{C_U \left(y_c - \frac{y_v}{2} \right)}{\kappa u_\tau}}{\frac{y_v}{\nu} + \frac{\ln\left(\frac{y_c}{y_v} \right)}{\kappa u_\tau}} \tag{14}$$

whereby $C_U = \frac{\partial U}{\partial t} + U \frac{\partial U}{\partial x} + V \frac{\partial U}{\partial y} + \frac{1}{\rho} \frac{\partial P}{\partial x}$ gathers momentum nonequilibrium terms (related, e.g., to the adverse or favorable pressure gradient).

Invoking the normalization definitions (Equations (12) and (13)), the generalized wall shear stress expression (Equation (14)) can be rewritten in the standard *log-law* form:

$$U^+_{log_\psi} = \frac{1}{\kappa\psi} ln(Ey^+) \tag{15}$$

by which the common value of the effective viscous sublayer thickness $y^+_v = 11$ recasts into the widely adopted logarithmic constant value $E = 8.9$ in the standard log-law, while $\psi = 1 - \dfrac{C_U\left(y_c - \dfrac{y_v}{2}\right)}{U_c \kappa u_\tau}$ is the nonequilibrium factor. As the linearization of the nonequilibrium effects encompassed by ψ in the derivation of Equation (14) might affect the stability, the bounding $\psi_{min} < \psi < \psi_{max}$ is considered.

One can note the equivalency between Equations (14) and (11), since in the equilibrium flow conditions $C_U = 0$ yields $\psi = 1$, and Equation (15) boils down to U^+_{log} for $y_c > y_v$ (coarse mesh). On the other hand, for $y_c < y_v$ (fine mesh), the velocity profile integration (Equation (14)) does not go beyond the viscous sublayer; hence, on the right-hand side, both in the nominator and the denominator, the second term is eliminated, and the τ_w expression is reduced to U^+_{vis}.

On a coarse mesh, the resolution near the wall is insufficient for the correct reconstruction of the velocity profile. Hence, to impose the correct wall shear stress in the momentum equation, the effective momentum diffusivity at the wall ν^{wall}_{eff} is derived from the WF expression (Equation (14)), accounting for the locally available wall-normal velocity gradient:

$$\begin{aligned} \tau_w &= \rho \nu^{wall}_{eff} \frac{U_c}{y_c} \\ \tau^+_w = 1 &= \frac{\nu^{wall}_{eff}}{\nu} \frac{U^+}{y^+} \\ \nu^{wall}_{eff} &= \nu \frac{y^+}{U^+} \end{aligned} \tag{16}$$

which comes to be the consistent formulation both for the ItW and WF cases. Namely, Equation (11) in the viscous sublayer $U^+ = y^+$ yields $\nu^{wall}_{eff} = \nu$, and in the logarithmic layer, $U^+ = \frac{1}{\kappa\psi} ln(Ey^+)$ gives $\nu^{wall}_{eff} = \frac{\kappa\psi u_\tau y}{ln(Ey^+)}$, provided there is an appropriate normalization (Equations (12) and (13)) and correct U^+ distribution throughout the near-wall region from CWT.

The mathematical requirement for CWT is to satisfy the limit condition: in the respective velocity region where its flow effect is dominant, the unified profile has to yield the limiting U^+_{vis} or U^+_{log} as the prevailing value (Equation (11)). This is a minor issue when the prevailing flow effect exists: the problem arises in bridging the buffer region between two distinct regions (approximately $5 < y^+ < 30$ in the boundary layer), since, in between, both effects are of equal importance. In mathematics, it is appropriate to work with harmonic means when the average ratios are desired, as is the case here to quantify the intensity of one flow effect over the other. In that view, for the blending of the two limiting normalized velocity definitions, a generalized harmonic mean is put forward (blue line in Figure 1a):

$$U^+_{blend} = \left[\frac{1}{\left(\frac{1}{U^+_{vis}}\right)^{n_b} + \left(\frac{1}{U^+_{log}}\right)^{n_b}} \right]^{1/n_b} \tag{17}$$

where the blending coefficient $n_b = 10/3$ is obtained by minimizing the root-mean-square difference between the velocity blending expression and the available reference velocity data (red symbols in Figure 1).

In addition to the unified velocity distribution (Equation (17)), the wall-normal velocity gradient is also sought from CWT, since the turbulent kinetic energy production reduces to $\mathcal{P}_c = |\overline{uv}|(dU/dy)$ in the homogeneous boundary layer, while the Reynolds shear stress is related to the turbulent kinetic energy $|\overline{uv}| = c_\mu^{1/2} k$ (Equation (13)). The wall-normal velocity gradients from Equation (11) are derived as the limiting values for the respective flow regions (green dotted and dash-dotted lines in Figure 1b for the inner and outer flow regions, respectively):

$$\frac{dU^+}{dy^+} = \begin{cases} \left(\frac{dU^+}{dy^+}\right)_{vis} = 1 & \textit{viscous sublayer} \\ \left(\frac{dU^+}{dy^+}\right)_{log} = \frac{1}{\kappa y^+} & \textit{logarithmic layer} \end{cases} \tag{18}$$

whereas the analytical differentiation of the blended velocity profile (Equation (17)) leads to the following expression for the blended wall-normal velocity gradient (blue line in Figure 1b):

$$\left(\frac{dU^+}{dy^+}\right)_{blend} = U_{blend}^{+\,(n_b+1)} \left[\frac{\frac{U_{vis}^{+\,n_b}}{\kappa} + U_{log}^{+\,(n_b+1)}}{U_{vis}^{+\,(n_b+1)} U_{log}^{+\,(n_b+1)}} \right]^{1/n_b} \tag{19}$$

which confirmed the best fit against the available reference velocity gradient data (red symbols in Figure 1b) with $n_b = 10/3$.

For the kinetic energy and the normalized fluctuating velocity, the wall boundary conditions $k_w = 0$ and $\zeta_w = 0$ follow directly from the kinematic requirement for the wall velocity fluctuations (no-slip). Here, the diffusive flux through the walls is eliminated by adjusting the respective diffusivity coefficient (analogous to imposing the effective diffusivity for the momentum). For the dissipation rate and relaxation function, however, the wall boundary conditions ε_w and f_{0_w} are obtained from the near-wall analysis of the transport equations for k and ζ, respectively, (expressed in terms of the values at the near-wall cell center).

On the coarse mesh, the cell-center value ε_c is assumed to be in equilibrium with the turbulent kinetic energy production $\mathcal{P}_c = \frac{c_\mu^{3/4} k_c^{3/2}}{\kappa y_c} = \varepsilon_c$, and for both quantities, this value is to be fixed in the center of the wall-adjacent cell. As for $\mathcal{P}$, this represents a satisfactory approximation throughout the near-wall region. However, ε is not in equilibrium with $\mathcal{P}$ very close to the wall: instead, there, it is balanced with the diffusion of k. Therefore, the exact wall boundary condition ε_w is to be imposed at the wall surface of the fine mesh $\varepsilon_w = \frac{2\nu k_c}{y_c^2}$. An effective way to reconcile these two wall treatment rationales (the definition at the wall surface and in the near-wall cell center) is to fix the blended value in the center of the near-wall cell:

$$\varepsilon_{blend} = \varepsilon_w \Gamma + \varepsilon_c (1 - \Gamma) \tag{20}$$

where, for the blending factor $\Gamma = (dU^+/dy^+)_{blend}$, the normalized velocity gradient can be used (Equation (19)) because of its transition between the inner and outer layer (Figure 1b: it goes to unity for small y and tends to zero for large y). This gives, for the blended value, the equilibrium definition at large y (coarse mesh), and at small y (fine mesh), it tends to the wall value with the assumed zero gradient (no diffusive flux).

Looking at the wall boundary condition for the relaxation function, its form is the same as the ε wall boundary condition, and it can be tuned to zero value through the appropriate selection of N_ζ:

$$f_{0_w} = (N_\zeta - 2) \frac{2\nu\zeta_c}{y_c^2} \tag{21}$$

whereby this same definition can be taken as the wall boundary condition irrespective of the distance from the wall of the near-wall cell center, on the grounds that the wall

blocking effect (that f_0 represents) decreases sharply with the distance to the wall, just like Equation (21) will tend to zero with increasing y.

Compared with the starting modeling approach [13], the presented $\zeta - f_0$ formulation of the elliptic relaxation function (Equations (7) and (8)) yields the wall boundary condition (Equation (21)) that ensures the model robustness despite the mesh quality and resolution insufficiency. Furthermore, unlike in the original idea [14], the compound wall treatment presented here (Equation (17)) provides a smooth and accurate transition between the inner and outer scaling. This physically sound near-wall strategy enables stable inclusion of the nonequilibrium near-wall flow effects (Equation (15)) and ensures the robustness of the numerical simulation with respect to the near-wall mesh quality.

3. Results

The ability of the deployed physical description to capture near-wall flow phenomena can be seen from recovering the underlying flow effects. For this purpose, both the $\zeta - f_0$ model (Equations (4)–(10)) and CWT near-wall treatment (Equations (11)–(21)) were implemented into the open-source CFD library suite *OpenFOAM* [20,21]. Subsequently, the presented turbulence modeling approach was validated on the generic test flow cases, which are representative of the flows featuring the principal wall-bounded flow phenomena: wall boundary layer, flow separation, recirculation and reattachment, and impingement and streamline curvature. The analyzed test cases were extensively examined experimentally and/or numerically, and the reference data were taken from the best available sources: either measurements or direct numerical simulation (DNS).

As the reference data for fully developed turbulent channel flow (Figure 2b), the DNS results with $Re_\tau = 800$ were used [22]. The backstep flow configuration $H/h = 4$ based on the step height h and the bulk velocity Reynolds number Re_h = 28,000 was analyzed (Figure 2d), and the results are compared with the available experimental data [23]. The impinging jet with a distance to plate $H/D = 2$ was simulated with the bulk velocity Reynolds number Re_D = 23,000 based on the pipe diameter D (Figure 2f) and compared with the experimental studies [24,25].

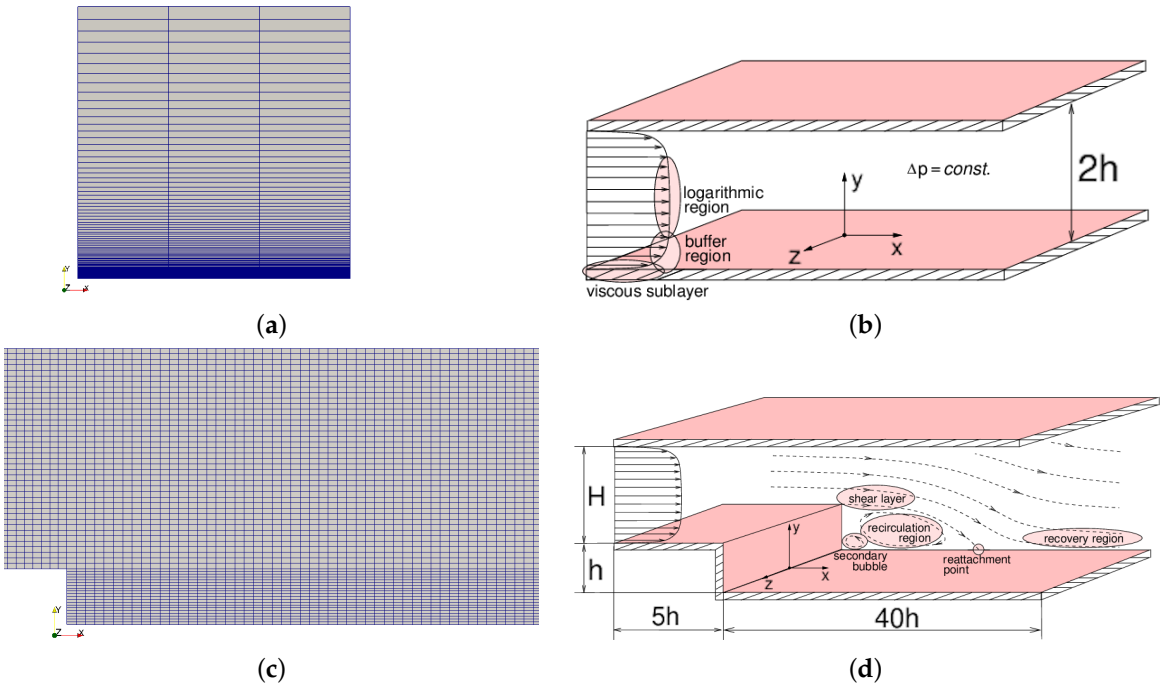

Figure 2. *Cont.*

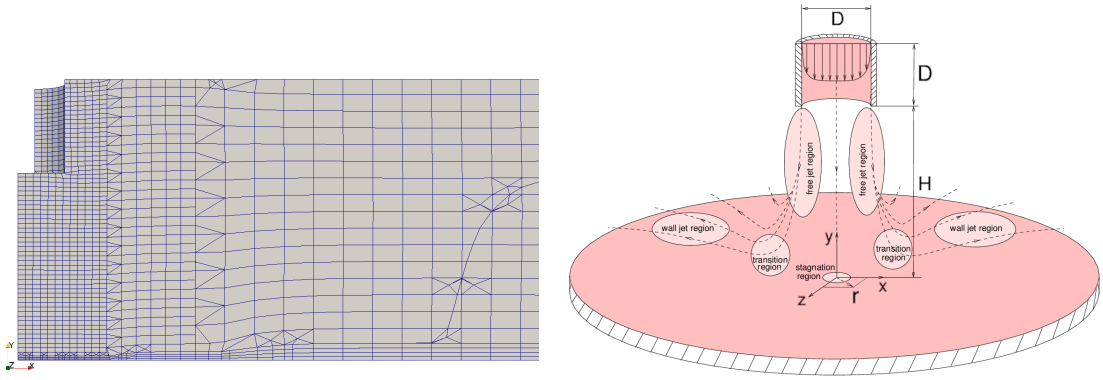

(**e**) (**f**)

Figure 2. The sections of the meshes (**left**) used for the simulation of the generic test flow cases (**right**): (**a**,**b**) plane channel flow; (**c**,**d**) backward-facing step flow; and (**e**,**f**) axisymmetric impinging jet.

3.1. Plane Channel Flow

In a simple parallel-plate channel geometry, the fully developed turbulent steady-state flow has nonhomogeneity in the wall-normal direction only (Figure 2b). With a constant streamwise pressure gradient driving this shear flow, the streamwise and spanwise gradients of the statistical quantities are zero, and modeling is needed to reconstruct the turbulence generation near the wall.

Figure 2a shows regular numerical mesh, which is used for the plane channel simulations. By changing the mesh clustering, the wall-adjacent cell center is placed in the viscous, buffer, and log-law region ($y^+ = 1, 10, 30$ respectively), putting CWT to test. The obtained normalized velocity (Figure 3a) and turbulent kinetic energy (Figure 3b) recover DNS wall-normal profiles well in case the cell center is in the viscous or log-law region ($y^+ = 1$ and $y^+ = 30$ mesh, respectively). When the cell center is located in the buffer region ($y^+ = 10$ mesh), even if the velocity in the wall-adjacent cell is captured well, there are not enough computational points throughout the near-wall region to reconstruct the steep velocity variation there, resulting in somewhat overpredicted wall shear stress (following the explanation of Equation (16)).

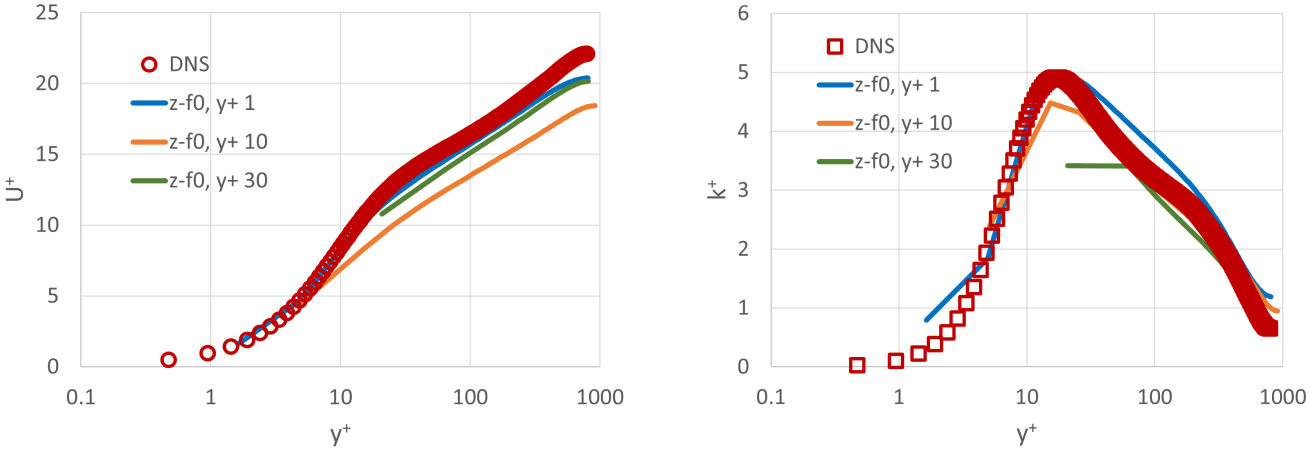

(**a**) (**b**)

Figure 3. Plane channel flow DNS results (symbols) and $\zeta - f_0$ simulations with different mesh clustering (lines): wall-normal distribution of the (**a**) normalized velocity and (**b**) normalized turbulent kinetic energy.

3.2. Backward-Facing Step Flow

As the incoming stream flows over a sharp step, it separates on its edge and creates the recirculation zone underneath. The resulting flow pattern, including the position of the reattachment point and the subsequent flow recovery, depend on the incoming flow characteristics and the geometry configuration (Figure 2d).

From the profiles of the streamwise velocity (normalized with the inlet bulk velocity) taken at different distances from the step (Figure 4), one can see that the flow pattern in the recirculation zone is reconstructed well, and the reattachment length prediction is good. It can be noted, though, that in the recovery zone, the flow develops somewhat more slowly. With the deployed mesh structure (Figure 2c), the average y^+ at the bottom wall was kept around 100; however, it inevitably changes due to the variation in the streamwise flow conditions. Nevertheless, the proposed near-wall treatment (Equation (17)) assures the correct wall boundary condition definition, regardless of the near-wall mesh resolution.

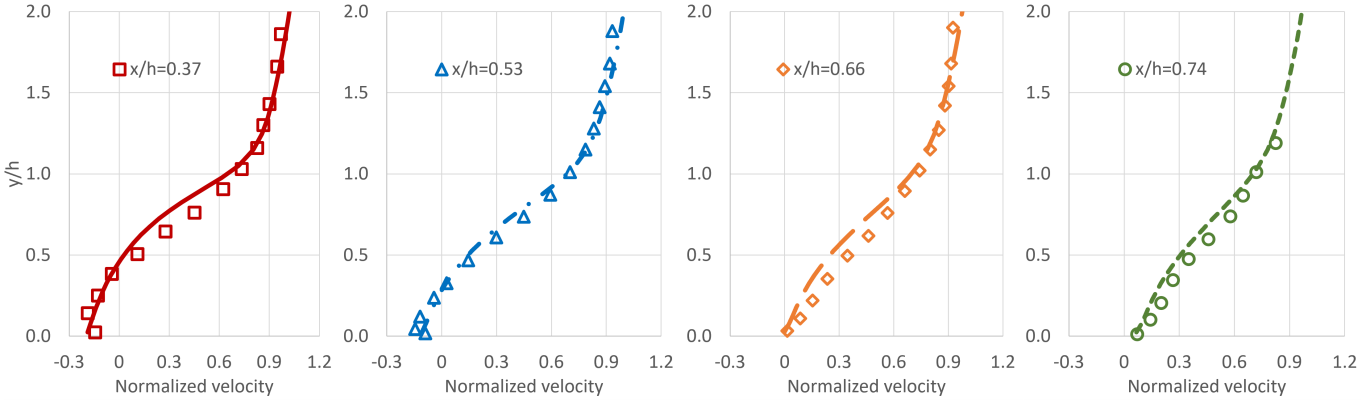

Figure 4. Backward−facing step flow experiments (symbols) and $\zeta - f_0$ simulations (lines): wall-normal distribution of the streamwise velocity normalized with the bulk velocity at the streamwise distance $x/h = 0.37, 0.53, 0.66, 0.74$ from the step.

3.3. Axisymmetric Impinging Jet

In a fully developed axisymmetric jet impinging into a plate, the streamline curvature effects are dominant. Flowing onto a target wall under the right angle, it generates the cylindrical shear layer (separating the jet core from the entraining ambient fluid), and in the stagnation region, the axial flow decelerates and deflects it into the radial wall jet (Figure 2f).

The mesh resolution was intentionally kept insufficient for an adequate reconstruction of the near-wall flow pattern (Figure 2e) in order to test the capability of the turbulence model. From the obtained profiles of the velocity magnitude normalized with the bulk velocity, obtained at different radial distances from the jet axis, shown in Figure 5, good agreement is observed in the stagnation region. However, in the wall jet region, the shear layer could not be resolved sufficiently: although the velocity profiles are recovering the main flow features, for a better reconstruction of the flow gradients, a finer mesh resolution is required. What proves the robustness of the model, however, is that during the flow development phase, the simulation was running stably. The full convergence was smoothly reached, which is not a common experience with other models: very often, a careful flow initialization is required (and/or low under-relaxation parameters) to stabilize the numerical process involving rapid flow variations.

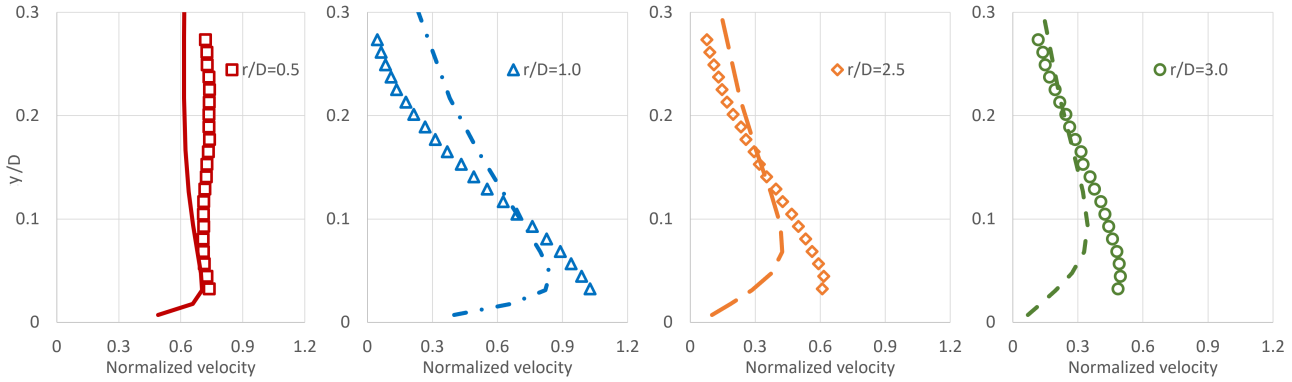

Figure 5. Axisymmetric impinging jet experiments (symbols) and $\zeta - f_0$ simulations (lines): wall-normal distribution of the velocity magnitude normalized with the bulk velocity at the radial distance $r/D = 0.5, 1.0, 2.5, 3.0$ from the jet axis ($r = \sqrt{x^2 + z^2}$).

4. Conclusions and Discussion

The modeling of the near-wall flow effects has a decisive role for the accurate prediction of wall-bounded flow characteristics. In this paper, a turbulent modeling framework is presented, which reproduces nonviscous pressure wall blocking effects (through f_0), the viscous damping of turbulent fluctuations (using ζ), and the dissipation adjustment (in ε equation) very close to the wall. In order to provide the numerical stability of the model, time and length scale constraints are used. The numerical parameters that control the simulation can be appropriately selected for the given flow conditions and mesh, and the relaxation function wall boundary condition can be tuned to zero in order to improve the simulation performance.

For robust simulations of complex engineering flows, the presented turbulent modeling framework incorporates a physically sound near-wall treatment, which handles arbitrary mesh quality and clustering. Namely, while a fine mesh resolution of the boundary layer allows for imposing the exact wall boundary conditions (ItW), with insufficient near-wall mesh resolution, the flow effect approximation is reconstructed from the boundary layer assumptions (WF). To enable seamless switching in the turbulence modeling operation regardless of the near-wall mesh characteristics, CWT based on the generalized harmonic mean provides accurate and continuous variation of turbulent quantities between their limiting definitions (ItW on fine mesh, WF on coarse mesh) throughout the near-wall region. It is important to note, however, that the physical correctness of the turbulence model with near-wall treatment cannot compensate the numerical requirement for resolving the fluid flow gradients.

Inspecting more deeply the adopted blending through the generalized harmonic mean, it is observed that the outer log-layer (log-law) is somewhat analogous to the inertial subrange of Kolmogorov [15]: the momentum transfer undergoes the transition from the outer, over the intermediate, towards the inner region—the same as when the turbulent energy cascades from large to small scales over the energy-containing inertial subrange. The energy spectrum describes a transfer of energy from low to high wavenumbers $\mathcal{K}$ through the energy cascade $\mathsf{E}(\mathcal{K}) = C_{\mathsf{E}}\varepsilon^{m_{\mathsf{E}}}\mathcal{K}^{n_{\mathsf{E}}}$, and numerous investigations have confirmed the negative slope of the velocity fluctuations spectrum $n_{\mathsf{E}} = -5/3$ [26]. Similarly, the pressure fluctuations in a turbulent flow can be characterized as $\mathsf{P}(\mathcal{K}) = C_{\mathsf{P}}\varepsilon^{m_{\mathsf{P}}}\mathcal{K}^{n_{\mathsf{P}}}$, and the pressure fluctuations spectrum falls off as $n_{\mathsf{P}} = -11/3$ in the inertial subrange of the shear flow [27]. On the other hand, the generalized harmonic mean can be conveniently reformulated as $(U^+_{blend})^{n_b} = (U^+_{vis})^{n_b} + (U^+_{log})^{n_b}$ for the negative exponent $n_b = -10/3$, which yielded the best fit with the reference data. It is worth noting that the blending exponent value corresponds to the turbulence cascade slope coefficient range for the observed turbulent fluctuations, which can be an indication that similar interaction mechanism guides the transition between the inner (viscous) and outer (logarithmic) flow distribution.

Funding: The presented work was supported through the Horizon Europe project NextETRUCK (Grant agreement ID: 101056740).

Data Availability Statement: The data presented in this study are available on request from the corresponding author.

Acknowledgments: The author expresses deep gratitude to his fluid dynamics teachers, Prof. Dr. Ismet Demirdžić and Prof. Dr. Kemal Hanjalić.

Conflicts of Interest: The author declares no conflict of interest.

Nomenclature

The following symbols are used in this paper to denote variables and constants and as subscripts:

Variables	
U_i	mean flow velocity vector
P	mean flow pressure
k	turbulent kinetic energy
ε	turbulent kinetic energy dissipation rate
$\mathcal{P}$	turbulent kinetic energy production
ζ	normalized fluctuating velocity
f_0	elliptic relaxation function (zero wall BC)
ρ	fluid density
ν	kinematic fluid viscosity
ν_t	kinematic turbulent viscosity
ν_{eff}	effective momentum diffusivity
$\mathcal{T}$	characteristic turbulent time scale
$\mathcal{L}$	characteristic turbulent length scale
$\mathcal{V}$	characteristic turbulent velocity scale
S_{ij}	rate-of-strain tensor
τ_w	wall shear stress
$\overline{u_i u_j}$	turbulent stress tensor
$\overline{v^2}$	wall-normal turbulent stress component
U^+	normalized velocity
y^+	normalized wall distance
u_τ	friction velocity
ψ	nonequilibrium factor
C_U	linearized nonequilibrium term
Subscripts	
i, j, k	vector components in streamwise, wall-normal, and spanwise direction
c	value in the near-wall cell center
w	value at the wall surface
log	logarithmic layer
vis	viscous sublayer
Constants	
κ	Von Karman constant
E	logarithmic constant
c_μ	turbulent viscosity coefficient
ζ_{eq}	equilibrium normalized fluctuating velocity
N_ζ	wall boundary coefficient for f_0
n_{blend}	CWT blending coefficient
$\sigma_{variable}$	Prandtl number (in equation for given variable)
$C_{variable}$	model coefficients (in equation for given variable)

References

1. Lesieur, M.; Metais, O. New trends in large-eddy simulations of turbulence. *Ann. Rev. J. Fluid Mech.* **1996**, *28*, 45–82. [CrossRef]
2. Smagorinsky, J. General circulation experiments with the primitive equations. *Mon. Weather Rev.* **1963**, *91*, 99–165. [CrossRef]
3. Germano, M.; Piomelli, U.; Moin, P.; Cabot, W.H. A dynamic subgrid-scale eddy viscosity model. *Phys. Fluids A* **1991**, *3*, 1760–1765. [CrossRef]

4. Metais, O.M.; Lesieur, L. Spectral large-eddy simulation of isotropic and stably stratified turbulence. *J. Fluid Mech.* **1992**, *239*, 157–194. [CrossRef]
5. Chaouat, B. The State of the Art of Hybrid RANS/LES Modeling for the Simulation of Turbulent Flows. *Flow Turbul. Combust.* **2017**, *99*, 279–327. [CrossRef]
6. Kochkov, D.; Smith, J.A.; Alieva, A.; Hoyer, S. Machine learning–accelerated computational fluid dynamics. *Proc. Natl. Acad. Sci. USA* **2021**, *118*, e2101784118. [CrossRef]
7. Jones, W.; Launder, B. The prediction of laminarization with two-equation model. *Int. J. Heat Mass Transf.* **1972**, *15*, 301–314. [CrossRef]
8. Patel, V.C.; Rodi, W.; Scheuerer, G. Turbulence Models for Near-Wall and Low Reynolds Number Flow: A Review. *AIAA J.* **1985**, *33*, 1308–1318. [CrossRef]
9. Durbin, P.A. Near-wall turbulence closure modelling without 'damping functions'. *Theoret. Comput. Fluid Dyn.* **1991**, *3*, 1–13. [CrossRef]
10. Lien, F.S.; Kalitzin, G.; Durbin, P.A. RANS modelling for compressible and transitional flows. In *Proceedings of the Summer Program, Center for Turbulence Research*; Stanford University: Stanford, CA, USA, 1998; pp. 267–286.
11. Durbin, P.A. On the k-ε stagnation point anomaly. *Int. J. Heat Fluid Flow* **1996**, *17*, 89–90. [CrossRef]
12. Davidson, L.; Nielsen, P.V.; Sveningsson, A. Modifications of the v2-f model for computing the flow in a 3D wall jet. In *Turbulence Heat and Mass Transfer, 4*; Begell House: Danbury, CT, USA, 2003.
13. Hanjalic, K.; Popovac, M.; Hadziabdic, M. A robust near-wall elliptic relaxation eddy-viscosity turbulence model for CFD. *Int. J. Heat Fluid Flow* **2004**, *25*, 897–901. [CrossRef]
14. Popovac, M.; Hanjalic, K. Compound wall treatment for RANS computation of complex turbulent flows and heat transfer. *Flow Turbul. Combust.* **2007**, *78*, 177–202. [CrossRef]
15. Durbin, P.; Pettersson, R. *Statistical Theory and Modeling for Turbulent Flows*; Wiley: Hoboken, NJ, USA, 2001.
16. Boussinesq, J. Théorie de l'Ecoulement tourbillant. *Mem. Présentés Par Divers Savants Acad. Sci. Inst. Fr.* **1877**, *23*, 46–50.
17. Speziale, C.; Sarkar, S.; Gatski, T. Modelling the pressure–strain correlation of turbulence: An invariant system dynamic approach. *J. Fluid. Mech.* **1991**, *227*, 245–272. [CrossRef]
18. Launder, B.E.; Spalding, D.B. The numerical computation of turbulent flows. *Comput. Methods Appl. Mech. Eng.* **1974**, *3*, 269–289. [CrossRef]
19. Townsend, A.A. *The Structure of Turbulent Shear Flow*; Cambridge University Press: Cambridge, UK, 1976.
20. CFD Direct Limited. *OpenFOAM: The Open Source CFD Toolbox. Programmer's Guide Version 1906*; OpenFOAM Foundation Ltd.: London, UK, 2019.
21. Weller, H.G.; Tabor, G.; Jasak, H.; Fureby, C. A tensorial approach to computational continuum mechanics using object orientated techniques. *Comput. Phys.* **1998**, *12*, 620–631. [CrossRef]
22. Tanahashi, M.; Kang, S.; Miyamoto, S.; Shiokawa, S.; Miyauchi, T. Scaling law of fine scale eddies in turbulent channel flows up to $Re_\tau = 800$. *Int. J. Heat Fluid Flow* **2004**, *25*, 331–340. [CrossRef]
23. Vogel, J.; Eaton, J. Combined heat transfer and fluid dynamic measurements downstream of a backward-facing step. *ASME J. Heat Transf.* **1985**, *107*, 922–929. [CrossRef]
24. Baughn, J.W.; Shimizu, S. Heat transfer measurements from a surface with uniform heat flux and an impinging jet. *ASME J. Heat Transf.* **1989**, *111*, 1096–1098. [CrossRef]
25. Baughn, J.W.; Hechanova, A.E.; Yan, X. An experimental study of entrainment effects on the heat transfer from a flat surface to a heated circular impinging jet. *ASME J. Heat Transf.* **1991**, *113*, 1023–1025. [CrossRef]
26. Monin, A.S.; Yaglom, A.M. *Statistical Fluid Mechanics, Mechanics of Turbulence*; MIT Press: Cambridge, MA, USA, 1975.
27. George, W.K.; Beuther, P.D.; Arndt, R.E.A. Pressure spectra in turbulent free shear flows. *J. Fluid Mech.* **1984**, *148*, 155–191. [CrossRef]